Non uniform beam filling correction for the Doppler velocity measured by the WIVERN conically scanning radar

Alessandro Battaglia,[a] Riccardo Rabino,[b] Kamil Mroz,[c] Frederic Tridon,[b] Antonio Parodi,[d]

[a] *Department of Environment, Land and Infrastructure Engineering, Politecnico di Torino, Turin, Italy; Earth Observation Science Group, Department of Physics and Astronomy,University of Leicester, Leicester, United Kingdom*

[b] *Department of Environment, Land and Infrastructure Engineering, Politecnico di Torino, Turin, Italy*

[c] *National Centre for Earth Observation, University of Leicester, Leicester, United Kingdom*

[d] *CIMA Foundation, Savona, Italy*

Corresponding author: Riccardo Rabino, riccardo.rabino@polito.it

ABSTRACT: Existing and planned spaceborne radar missions offer unique three-dimensional views of clouds, precipitation, and convection, enhancing our understanding of Earth's water and energy cycles. Doppler and wide swath capabilities are now being considered as additional features to enhance radar capabilities. One such system is the ESA Wind Velocity Radar Nephoscope (WIVERN), currently in phase A studies; its payload consists of one conically-scanning Doppler W-band radar in low-Earth orbit, designed to measure the profile of the line-of-sight wind profile and the vertical structure of hydrometeor content. These observations are crucial for improving Numerical Weather Prediction models and evaluating cloud and precipitation processes in next-generation Earth System Models.

A significant error source in WIVERN's LoS Doppler velocities is the Non-Uniform Beam Filling (NUBF) error, introduced by reflectivity field inhomogeneities within the backscattering volume. This effect has been studied for nadir-looking Doppler radars, like EarthCARE. This work proposes a methodology to reduce such error which is applicable to WIVERN's conically-scanning configuration. Depending on the antenna pointing with respect to the satellite velocity, the correction is proportional to spatial reflectivity gradients in directions which are not necessarily sampled by the scanning pattern. End-to-end simulations of WIVERN for different storms show that NUBF errors depend on the antenna scanning-angle, are unbiased and generally have a standard deviation below 1 m/s. The NUBF correction can reduce this error by approximately 40%, though its effectiveness decreases when accounting for the reflectivity measurements noisiness. Errors from wind shear are smaller, but the proposed mitigation schemes are less effective due to the Doppler velocity and reflectivity measurements combined noisiness.

SIGNIFICANCE STATEMENT: Future satellites in low Earth orbit are expected to deploy radars with Doppler capabilities and slant looking view to study the dynamic of the Earth's cloud systems. Uncertainties in measured Doppler velocities are usually required to be less than a few m/s to meet mission requirements. However, Doppler velocity errors increase in regions where there is reflectivity inhomogeneity within the backscattering volume due to the apparent wind shear introduced over the same volume by the rapid motion of the satellite. This work proposes a technique that successfully mitigates this error to uncertainties lower than 1 m/s by extending the methodology developed for nadir-looking to conically-scanning radars.

1. Introduction

Space-borne Doppler radars represent a new paradigm in radar meteorology, which promises unprecedented capabilities for studying atmospheric dynamics, cloud microphysics and precipitation processes from space (Durden et al. 2016; Tanelli et al. 2018; Battaglia et al. 2020; Kollias et al. 2022a). First data from the EarthCARE W-band nadir-looking Cloud Profiling Radar (CPR), the first atmospheric radar with Doppler capabilities (Illingworth et al. 2015; Kollias et al. 2014, 2022b), confirm that it will be possible to map vertical movements of hydrometeor in the troposphere on a global scale (Galfione et al. (2025)).

When dealing with Doppler radars, the transition from ground-based to low-Earth-orbiting (LEO) configurations introduces several technical and scientific challenges that must be addressed to ensure accurate and reliable measurements. The main problem is related to the intrinsic nature of the Doppler measurements, i.e. phase shifts are the result of the relative motion between the measuring system and the observed targets, coupled with the fast motion of the instrument ($\approx$ 7.6 km/s), which is three orders of magnitude larger than typical hydrometeor velocities when measured from an Earth-fixed reference of frame. This has two main consequences:

1. the motion of the radar platform, coupled with the finite antenna beamwidth, causes a significant broadening of the Doppler spectrum (of the order of 3-4 m/s with typical beamwidths) due to the different values of the satellite velocity projections in different parts of the footprints, a phenomenon referred to as "Doppler fading" (Tanelli et al. 2002; Kobayashi et al. 2002; Battaglia et al. 2013);

2. any small error in the antenna pointing translates into a Doppler velocity error (Tanelli et al. 2014; Battaglia and Kollias 2014). Recent studies demonstrate that, even when considering fast rotating antennas, the determination system can achieve an absolute knowledge error under 100 μrad per axis in terms of attitude (Manconi et al. 2025) whereas thermo-elastic effects can be corrected down to residual less than 0.15 m/s by using natural target calibration techniques (Treserras et al. 2025).

The first problem has two far-reaching implications.

Firstly, large spectral widths significantly lower the radar decorrelation times (Kobayashi et al. 2002; Battaglia and Kollias 2015). This degrades the quality of the Doppler velocity, unless very high pulse repetition frequencies (PRF) and long integration times are used (as adopted for the EarthCARE CPR, Treserras et al. (2025)). However, a high PRF can be detrimental for sampling the full troposphere (e.g. presence of second trip echoes as predicted by Battaglia (2021) and confirmed during the EarthCARE commissioning phase).

Secondly, the Doppler velocities are biased when the radar beam encounters inhomogeneities in the precipitation or cloud structures within the resolution volume, i.e. in the presence of non-uniform beam filling (NUBF). Since Doppler velocities are reflectivity weighted, if the radar beam is not uniformly filled, the measured Doppler velocity will be biased towards the apparent relative velocity of the brighter scatterers within the beam. Even in the presence of uniform winds and hydrometeors with the same sedimentation velocity within the radar backscatter volume, platform motion introduces significant Doppler fading within the footprints. This bias can be large (several m/s) because LEO radars have a large backscattering volume, thus increasing the likelihood of encountering non-uniform structures like cloud and precipitation edges. This effect is further exacerbated in presence of strong wind shears and/or sedimentation velocity gradients. Overall NUBF errors can significantly contribute to the overall error budget of Doppler velocity measurements from fast-moving platforms (Battaglia and Kollias 2015; Kollias et al. 2022a). Thus accurate corrections of NUBF effects are essential for improving the quality of space-borne Doppler radar data.

The recently launched Earth Cloud Aerosol and Radiation Explorer (EarthCARE) mission, equipped with a nadir-looking W-band CPR (Illingworth et al. 2015), is designed to study convective and sedimentation motions and cloud properties. Since the Doppler velocity measurements are susceptible to NUBF effects, numerous studies have developed robust corrections to mitigate their impact on scientific data Tanelli et al. (2002); Schutgens (2008); Sy et al. (2014); Kollias et al. (2014). All these corrections are based on the gradient reflectivity method, i.e. the bias correction applied to the Doppler velocity is proportional to the along-track reflectivity gradient. The assumption underpinning the method is that the reflectivity gradient within the backscattering volume can be estimated from the large scale reflectivity spatial gradient. The correction is currently being tested with EarthCARE data.

The challenges associated with NUBF become even more pronounced for slant-looking Doppler radars, such as for the proposed WIVERN (Wind Velocity Radar Nephoscope) mission. WIVERN, one of the two finalists of the ESA's Earth Explorer 11 programme, represents a revolutionary concept in Earth's observations. It features a W-band cloud radar with a large reflector that is fast conically scanning at an off-nadir angle of about 38 degrees (Illingworth et al. 2018). This configuration allows WIVERN to measure horizontal wind speeds in clouds and precipitation and to map the three dimensional structure of mesoscale weather systems, thus providing a novel perspective for weather forecasting and mesoscale climate dynamics studies.

However, WIVERN conical scanning geometry introduces additional complexity to the NUBF correction. Unlike nadir-looking radars, where the satellite velocity vector is almost perfectly orthogonal to the radar beam, with conically scanning radars the orientation between the satellite velocity and the boresight direction changes rapidly as the radar performs a conical scan. This makes the NUBF Doppler velocity bias induced by the satellite motion a function of the scanning angle. Scope of this work is first to discuss the peculiarity of NUBF Doppler velocity bias for conically scanning configurations (Sect. 2). Then a correction algorithm that generalizes the methodologies developed for nadir-looking radars is introduced in Sect. 3. Sect. 4 presents results of simulations and expected performances of the corrections for the WIVERN radar configuration. Conclusions are drawn in Sect. 4.

2. NUBF for conically scanning radars

For a nadir looking radar the NUBF is illustrated in Fig. 1. All directions $\hat{\mathbf{u}}_r$ within the backscatter volume in the forward part of the footprint [i.e. where $\hat{\mathbf{u}}_{sat} \cdot (\hat{\mathbf{u}}_r - \hat{\mathbf{u}}_{BS}) > 0$] are characterized by positive (downward) velocities once the platform motion along the LoS, $\hat{\mathbf{u}}_{sat} \cdot \hat{\mathbf{u}}_{BS}$, has been

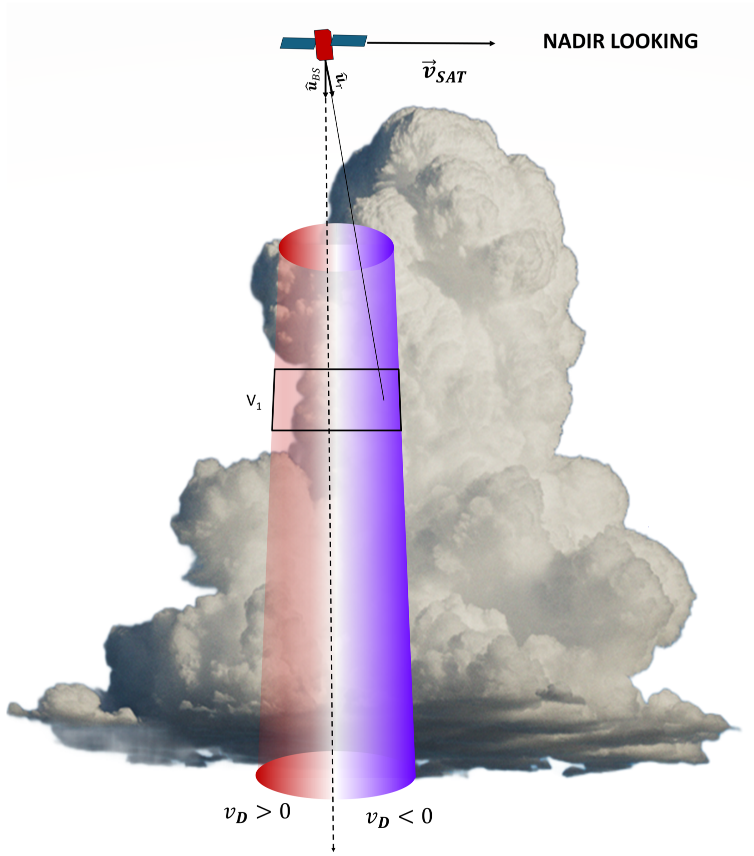

FIG. 1. Cartoon illustrating the NUBF problem for nadir-looking radars. The wind shear across the 3 dB footprint is illustrated by the color palette with Doppler velocity values ranging from ±5.8 m/s for the EarthCARE configuration. Red (purple) colors correspond to targets that are apparently receding from (approaching) the radar.

subtracted; this means that the hydrometeors will appear to be moving upward, i.e. approaching the radar (negative Doppler velocities). Correspondingly there will be a shift toward higher frequencies (violet shift). The intensity of the Doppler frequency shift will increase moving away from the boresight (color moving from white to deep violet). For instance for the EarthCARE satellite at the border of the 3 dB beamwidth the effect is of the order of 5.8 m/s. The exact opposite effect will occur in the backward part of the footprint (red shift, hydrometeors apparently receding from the radar). Along-track radar reflectivity gradients within the radar sampling volume introduces a bias in Doppler velocity estimates (Tanelli et al. 2002). For example, the backward part of the

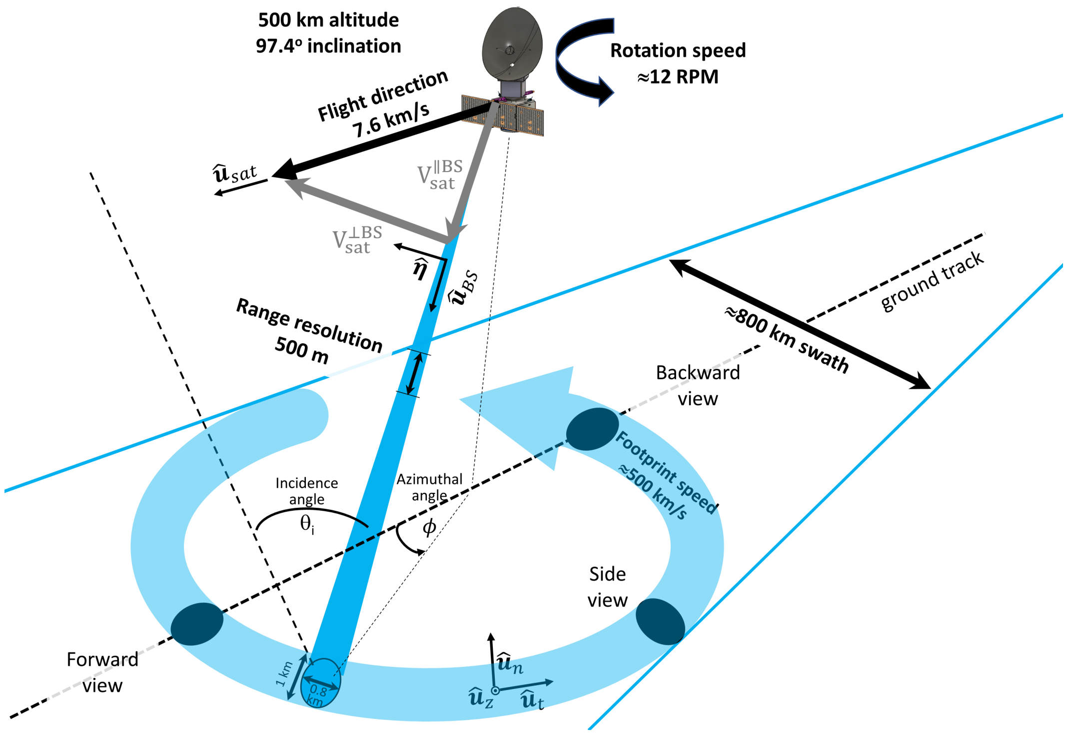

FIG. 2. Conically scanning geometry envisaged for the WIVERN mission with unit vectors and angles used in the text. The width of the footprint is exaggerated for illustration purposes.

backscatter volume V_1 is only partially filled by hydrometeors; this implies that the mean Doppler velocity will be biased toward the negative values of the forward part of the backscatter volume.

The situation complicates when dealing with conically scanning radar systems like the one envisaged for the WIVERN mission. The geometry of observation together with the main specifics of the WIVERN radar are illustrated in Fig. 2. If funded, WIVERN will deploy a dual-polarization Doppler W-band conically scanning cloud radar with a large elliptical non-deployable main reflector. WIVERN antenna scans at an off-nadir angle of 38° (which corresponds to an incidence angle of approximately 42°) at 12 revolutions per minute. Such a speed rotation implies the use of one horn for transmission and the other for reception, allowing for continuous scanning without the need for mechanical switching. The radar has Doppler capability, with Doppler measurements obtained using the polarisation diversity pulse-pair approach (Pazmany et al. 1999; Battaglia et al. 2013) and will transmit pair of H and V-polarized pulses separated by 20 μs every 250 μs (see Battaglia et al. (2025), their Fig 2). The scanning position can be characterized by the azimuthal scanning

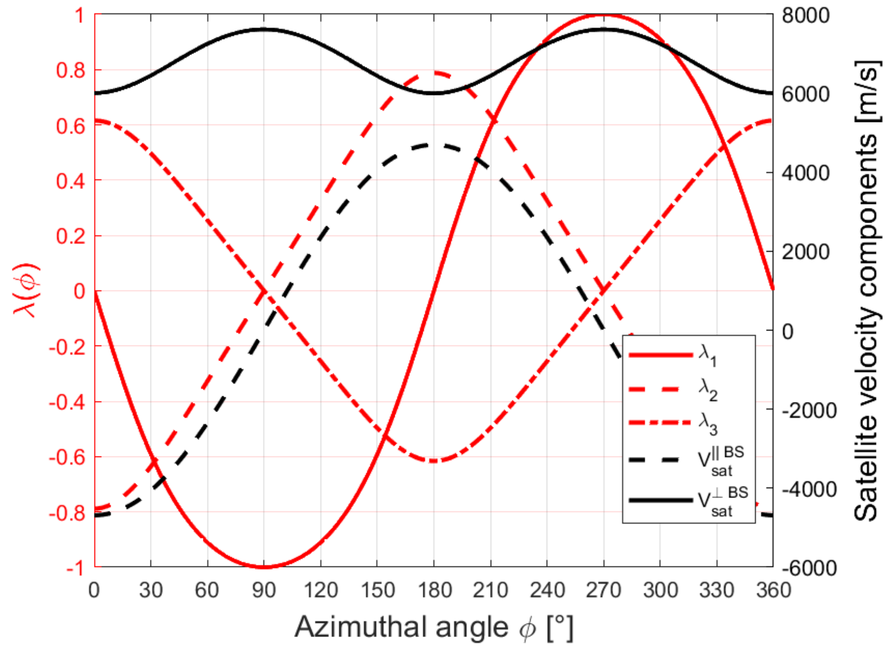

FIG. 3. Behaviour of λ_1, λ_2 and λ_3 (left y-axis) as a function of the azimuthal angle from 0° to 360°. The diagram also shows the projected satellite velocity along the boresight and orthogonal to it (right y-axis).

angle, ϕ, which is measured counterclockwise from the forward view; therefore, $\phi = 0°$, $\phi = \pm 90°$ and $\phi = 180°$ correspond to the forward, side (right and left) and backward views, respectively.

As the antenna rotates the angle between the antenna boresight (BS), $\hat{\mathbf{u}}_{BS}$, and the satellite velocity $\mathbf{V}_{sat}$ changes. This has two consequences:

1. There is a component of the satellite velocity along the antenna boresight (BS) direction, $V_{sat}^{\parallel BS}$, that is changing with ϕ between -4.7 to +4.7 km/s moving from forward to backward direction (see dashed black line in Fig. 3). This velocity produces a large Doppler shift (of the order of ±3 MHz) that must be perfectly compensated at each pulse. This can be done digitally at the receiver level.

2. The wind shear introduced within the radar backscattering volume by the satellite motion changes with the azimuthal scanning angle. The isodop contours (level of constant Doppler velocities), illustrated by the color palette in Fig. 4 for two azimuthal angles (left panel: forward; right panel: side), clearly show a rotation when moving from forward to side view.

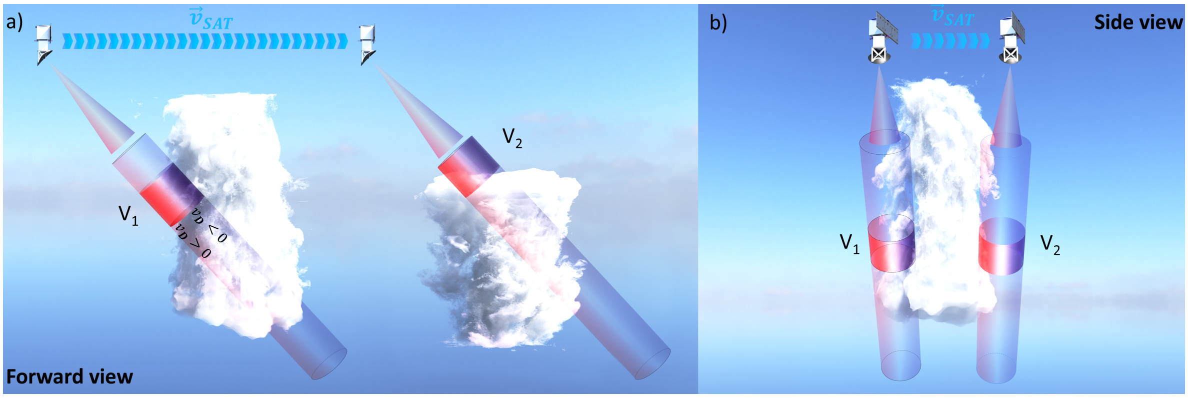

FIG. 4. Cartoon explaining Doppler velocity errors introduced by NUBF for slant looking radars. Panel a): forward-looking view; panel b): side-looking view. In both cases the satellite is moving from left to right. The wind shear across the 3 dB footprint projected on a plane orthogonal to the LoS is illustrated by the color palette ranging from ±3.7 m/s in the forward/backward view and ±4.6 m/s at side view. Red (violet) colors correspond to receding (approaching) velocities and lower (higher) frequencies of the backscattered radar signal. Rendering by P. Ercole-Cavatore.

> Note that the shear is larger at side view because in that condition the satellite velocity perpendicular to the boresight, $V_{sat}^{\perp BS}$, is maximum (see the dashed black line in Fig. 3). When this shear is coupled with reflectivity inhomogeneities within the backscattering volume (like for volume V_1 or V_2 in Fig. 4), biases in the Doppler velocities will arise.

The left panel of Fig. 4 demonstrates what happens when considering backscattering volumes astride cloud sides (volume V_1) or cloud tops (volume V_2) for a forward looking radar. For V_1 the Doppler velocity will be violet-shifted (thus a negative Doppler velocity bias) whereas for V_2 it will be red-shifted (positive bias). In general for backward and forward views, biases will be linked to vertical gradients of radar reflectivities which are typically negative near cloud tops and positive at cloud bases (or in regions deep inside clouds where strong attenuation is encountered). For forward looking geometry, biases will be positive (negative) at cloud top (base); the situation is opposite when considering backward view.

On the other hand for side view (right panel of Fig. 4), biases will be associated to horizontal gradients of radar reflectivities which are typically encountered at the edges of clouds. For volume

V_1 (V_2) entering (exiting) a cloud side, a violet (red) shift i.e. a negative (positive) Doppler velocity bias will be produced.

These simple examples demonstrate that NUBF will affect the Doppler velocities in different ways for different scanning directions. It is also clear that when considering a large number of viewing directions the distribution of biases will tend, statistically, to have zero mean; for instance cloud tops will be seen statistically the same amount of times in the forward and in the backward direction, thus producing biases with opposite signs, that will statistically cancel out. Similarly, there will be an equal number of scan volumes entering and exiting cloud edges for side views. Thus, the nature of the conical scanning pattern causes the NUBF error distribution to have a zero mean by construction. This is very important for data assimilation, which is very sensitive to bias (Horanyi et al. 2014).

3. NUBF correction for conically scanning radars

a. Satellite motion NUBF error correction

For nadir-pointing radars, notional studies demonstrated that the biases introduced by the satellite motion NUBF effects can be mitigated by estimating the along-track reflectivity gradient because NUBF-induced biases are expected to be linearly proportional to such reflectivity gradients (Schutgens (2008); Kollias et al. (2014); Sy et al. (2014); Battaglia et al. (2020)). Similarly, in a slant-looking geometry (Battaglia and Kollias (2015)), the relevant gradients are those along the direction orthogonal to the boresight and lying in the plane containing the satellite velocity and the antenna boresight direction ($\hat{\eta}$ direction in Fig. 2). In a conical scanning system like WIVERN, it is more challenging to retrieve the reflectivity gradients along such directions for all azimuthal angles for two reasons.

1. The reflectivities averaged at 1 km integration length are very noisy (due to the fast footprint speed which is $\approx$ 500 km/s, only a limited number of pulses, less than 10, is available for averaging in the pulse pair processing). This will produce noisy estimates of reflectivity gradients.

2. The direction along which the gradient needs to be computed may not be fully sampled by the radar scanning patterns. For instance, when looking in the forward/backward direction,

the $\hat{\boldsymbol{\eta}}$ direction is a combination of the vertical and the horizontal components which are only partially sampled by the conical scanning pattern. On the other hand when looking sideways it involves a horizontal component which is fully sampled by the scanning pattern.

For Gaussian circular antennas, if the reflectivity field can be approximated to vary linearly within the backscattering volume, then the bias introduced by the satellite motion (defined as the difference between the Doppler velocities measured by an instrument on a moving platform and the same quantity measured by a still instrument) is equal to (Sy et al. (2014); Battaglia and Kollias (2015)):

$$\delta v_{NUBF} = v_{sat}^{\perp BS} \frac{\nabla_\eta Z}{4.343} \frac{1}{4r\ \log(2)} R_{3dB}^2 = v_{sat}^{\perp BS} \frac{\nabla_\eta Z}{4.343} \frac{r\,\theta_{3dB}^2}{16\ \log(2)} \tag{1}$$

where $R_{3dB} = \frac{r\,\theta_{3dB}}{2}$ is the radius corresponding to the 3-dB beamwidth, r is the range between the satellite and the ground along the boresight, and $v_{sat}^{\perp BS}$ is the ground-track satellite velocity orthogonal to the boresight, which varies along the scan as illustrated in Fig. 3 (continuous black line). Because in our convention positive (negative) Doppler velocities correspond to receding (approaching) particles, positive (negative) NUBF biases correspond to receding (approaching) velocities and will be plotted with warm (cold) colors. This is consistent with the astronomer red shifts due to the Universe's expansion.

The gradient along $\hat{\boldsymbol{\eta}}$ can be estimated from the gradient formula as:

$$\nabla_\eta Z = \vec{\nabla} Z \cdot \hat{\boldsymbol{\eta}} \tag{2}$$

which is true for any reference of frame. Now if we use a reference of frame with $(\hat{\mathbf{u}}_t, \hat{\mathbf{u}}_n, \hat{\mathbf{u}}_z)$ with $\hat{\mathbf{u}}_t$ tangential to the cycloid (counterclockwise), $\hat{\mathbf{u}}_n$ normal to the cycloid inward in the horizontal plane and $\hat{\mathbf{u}}_z$ along the local vertical (see Fig. 2), then for each position across the cycloid the unit vector $\hat{\boldsymbol{\eta}}$ can be written as:

$$\hat{\boldsymbol{\eta}} = \frac{\hat{\mathbf{u}}_{sat} - (\hat{\mathbf{u}}_{BS} \cdot \hat{\mathbf{u}}_{sat})\, \hat{\mathbf{u}}_{BS}}{|\hat{\mathbf{u}}_{sat} - (\hat{\mathbf{u}}_{BS} \cdot \hat{\mathbf{u}}_{sat})\, \hat{\mathbf{u}}_{BS}|} \tag{3}$$

where $\hat{\mathbf{u}}_{sat}$ is the unit vector in the direction of the satellite velocity and $\hat{\mathbf{u}}_{BS}$ is the antenna boresight unit vector. Then $\hat{\boldsymbol{\eta}}$ can be decomposed on the $(\hat{\mathbf{u}}_t, \hat{\mathbf{u}}_n, \hat{\mathbf{u}}_z)$ reference frame as

$$\hat{\boldsymbol{\eta}} = \lambda_1(\phi)\hat{\mathbf{u}}_t + \lambda_2(\phi)\hat{\mathbf{u}}_n + \lambda_3(\phi)\hat{\mathbf{u}}_z \tag{4}$$

where the coefficient λs are derived from the respective dot products with the unit vectors of the $(\hat{\mathbf{u}}_t, \hat{\mathbf{u}}_n, \hat{\mathbf{u}}_z)$ reference frame:

$$\lambda_1 = \hat{\boldsymbol{\eta}} \cdot \hat{\mathbf{u}}_t \tag{5}$$

$$\lambda_2 = \hat{\boldsymbol{\eta}} \cdot \hat{\mathbf{u}}_n \tag{6}$$

$$\lambda_3 = \hat{\boldsymbol{\eta}} \cdot \hat{\mathbf{u}}_z \tag{7}$$

and are a function of the azimuthal scanning angle, ϕ, as shown in Fig. 3. Note that, because of the symmetry associated with the conical scan, all coefficients assume both positive and negative symmetric values when ϕ ranges from 0° to 360°.

By using the expression (2) we get:

$$\nabla_\eta Z = \lambda_1 \nabla_{\hat{\mathbf{u}}_t} Z + \lambda_2 \nabla_{\hat{\mathbf{u}}_n} Z + \lambda_3 \nabla_{\hat{\mathbf{u}}_z} Z \approx \lambda_1(\phi) \nabla_{\hat{\mathbf{u}}_t} Z + \lambda_3(\phi) \nabla_{\hat{\mathbf{u}}_z} Z \tag{8}$$

where the approximation is forced by the fact that for WIVERN it is not possible to estimate $\nabla_{\hat{\mathbf{u}}_n} Z$. Only at side view (when the $\hat{\boldsymbol{\eta}}$ direction is actually parallel or antiparallel to $\hat{\mathbf{u}}_t$) the λ_2 term will be identically zero. On the other hand, its impact will be maximal in the forward/backward view. Viceversa the effect coming from the vertical reflectivity gradient term contributing to $\nabla_\eta Z$ in Eq. 8 can be accounted for (though it will have a maximum impact in the forward/backward configuration and no effect in a side view) based on the assumption that the vertical changes of reflectivities dominate the along range gradients so that the vertical gradients can be inferred from $\nabla_{\hat{\mathbf{u}}_z} Z = \nabla_{\hat{\mathbf{u}}_r} Z / \cos(\theta_i)$ where $\hat{\mathbf{u}}_r$ is directed from the surface to the satellite along the BS direction.

By inserting Eq. (8) into Eq. (1) for a circular antenna the $NUBF$ bias can be expressed as:

$$\delta v_{NUBF} = v_{sat}^{\perp BS} \frac{\lambda_1(\phi) \nabla_{\hat{\mathbf{u}}_t} Z + \lambda_3(\phi) \nabla_{\hat{\mathbf{u}}_z} Z}{4.343} \frac{r\, \theta_{3dB}^2}{16\, \log(2)} \tag{9}$$

If the antenna is not circular but elliptical with a horizontal and vertical beamwidth equal to θ^H_{3dB} and θ^V_{3dB}, respectively (equal to approximately 0.072 and 0.066 degrees for WIVERN) then Eq. (9) will read:

$$\delta v_{NUBF} = v_{sat}^{\perp BS} \frac{\lambda_1(\phi)\nabla_{\hat{\mathbf{u}}_t} Z(\theta^H_{3dB})^2 + \lambda_3(\phi)\nabla_{\hat{\mathbf{u}}_z} Z(\theta^V_{3dB})^2}{4.343} \frac{r}{16\,\log(2)} \tag{10}$$

Eq. (10) greatly simplifies at side view where $\lambda_2 = \lambda_3 = 0$ whereas at forward/backward looking angles ($\phi = 0, \pi$) $\lambda_1 = 0$. At side view (i.e. $\phi = \pm 90°$) only horizontal gradients are relevant (and are fully captured by the WIVERN measurements); the bias correction for $\theta_{3dB} = 0.072°$ and $r = 675$ km is approximately 0.27 ms^{-1} per dB km^{-1} of horizontal gradient. In the forward/backward view (that is, $\phi = 0,\ 180°$), the horizontal gradients will not be captured by the measurements and the correction will be driven by the vertical gradient and equal to approximately 0.20 ms^{-1} per dB km^{-1} of vertical gradient.

b. Wind shear NUBF error correction

Similarly to those introduced by satellite-motion, biases in the Doppler velocities measurements may arise when there is a vertical wind shear coupled with a large vertical gradient of radar reflectivity across the radar backscattering volume. Since the vertical wind shear is generally considerably larger than the horizontal one, under the assumption that the reflectivity and wind fields can be approximated to vary linearly within the backscattering volume, the bias due to wind shear (WS) can be approximated as (Battaglia et al. 2018):

$$\delta v_{WS} = \frac{\nabla_z Z\ \nabla_z v_{LoS}}{4.343} \left[\frac{\Delta r^2}{12} \cos^2\theta_i + \frac{r^2 \theta^2_{3dB}}{16\,\log(2)} \sin^2\theta_i \right] \tag{11}$$

where Δr is the radar range resolution, $\nabla_z Z$ and $\nabla_z v_{LoS}$ are the reflectivity and line-of-sight wind vertical gradients expressed in dB m^{-1} and in s^{-1}. For the "WIVERN" configuration this corresponds to a bias of 0.083 m s^{-1} per dB km^{-1} for a wind shear of 0.01 s^{-1}. The reflectivity gradients and wind shear along the vertical direction can be inferred from adjacent gates and therefore a correction can be attempted. Wind-shear-induced biases are generally smaller than NUBF-induced biases with amplitudes up to 1 m s^{-1} and confined to the areas at the edge of clouds characterized by large wind shear and vertical reflectivity gradients.

4. End to end simulations and NUBF corrections

An end to end simulator for the WIVERN mission has been developed and refined in the past four years. The backbone simulator, thoroughly described in Battaglia et al. (2022), has been recently updated with an $I\&Q$ (Battaglia et al. (2025)) and a surface clutter (Manconi et al. (2024)) module. The simulator can be applied to atmospheric scene outputs produced by cloud resolving models like WRF, SAM or ICON. The simulations produce slant profiles of reflectivity and Doppler velocity signals with the expected noisiness and sampling. Radar observables are computed first without noise by simply integrating the relevant quantities over the backscattering volumes. Doppler velocities are computed as the reflectivity averaged sum of the contributions coming from the surface clutter and from the hydrometeors by accounting for the hydrometeor Doppler terminal velocity and the wind speed along the line of sight viewing direction of the radar. Noise (with a single pulse sensitivity level assumed to be -18 dBZ) is then injected for producing $I\&Q$s according to the method described in Battaglia et al. (2025). From the $I\&Q$s reflectivity and Doppler velocities can be computed according to standard pulse pair processing (Pazmany et al. 1999). For the WIVERN configuration, typical errors as a function of signal-to-noise ratios (SNR) for reflectivities and Doppler velocities are described in Battaglia et al. (2025). In the following, noisy observables will be indicated with a tilde, e.g. $\tilde{Z}$.

All products are sampled every 167 m in range and averaged over 1 km in the scan direction. The reflectivity signals are further refined by eliminating crosstalk, following the methodology proposed by Rizik et al. (2023). Finally, a feature mask similar to the one currently used for the EarthCARE CPR (Kollias et al. (2022b)) is applied to identify significant cloud returns and clutter-contaminated regions.

The NUBF study is restricted to cloudy regions where the signal-to-clutter ratio exceeds 10 dB and where the signal to noise ratio exceeds 0 dB (i.e. reflectivities exceeding -18 dBZ, thus a Doppler with small errors as demonstrated in Battaglia et al. (2025)). The advantage of a simulator framework is that the different Doppler velocity error sources can be directly quantified (Battaglia et al. (2022)). At any given range r the estimate of the error caused by the NUBF is given by:

$$\Delta \mathrm{v}_{\mathrm{NUBF}}(r) = v_D^{\mathrm{atm}}(r) - v_{D0}^{\mathrm{atm}}(r) \tag{12}$$

where v_D^{atm} is the ideal (i.e. without noise) Doppler (i.e. reflectivity-weighted) Line of Sight (LoS) velocity and v_{D0}^{atm} is the LoS Doppler velocity computed in the same way as v_D^{atm}, but setting to zero the speed of the moving platform ($v_{sat} = 0$).

The error caused by wind shear can be estimated by computing the antenna weighted (AW) ideal velocities (i.e. not weighted by the reflectivity and without any noise) and comparing it with v_{D0}^{atm}:

$$\Delta \mathrm{v}_{\mathrm{WS}}(r) = v_{AW0}^{\text{atm}}(r) - v_{D0}^{\text{atm}}(r). \tag{13}$$

Here in both cases the satellite velocity is set to zero (“0” subscript) in order to isolate the contribution from the wind shear.

a. Savitzky Golay filtering for the computation of gradients

A key ingredient for the NUBF corrections is the computation of the vertical and along-track reflectivity and Doppler velocity gradients [see Eqs. (10-11)]. Since the reflectivities/Doppler velocities measured by WIVERN are expected to be noisy (of the order of 1.2-1.5 dB and 1-1.2 m/s, respectively at high SNR at 1 km integration) the reflectivity/Doppler velocity fields are first smoothed by a two-dimensional Savitzky-Golay (SG) filter (Savitzky and Golay 1964), which is a method used to reduce noise in data while keeping key characteristics of the signal. The filter uses a local data window and approximates the function with a polynomial (of second degree in our case) and then replaces the center point with the estimated value. The window is specified in terms of an (odd) number of vertical (n_V) and horizontal pixels (n_H). Since WIVERN samples every 1 km in the horizontal and 125 m in the vertical $n_H = 3, 5$ (i.e. 3 or 5 km averaging horizontally) $n_V = 3, \ldots, 9$ (i.e. 0.375-1.125 km averaging vertically) have been selected. These are sensible averaging regions for smoothing the reflectivity fields. The selection of the best (n_H, n_V) pairs is discussed below and results from the trade-off between reducing the noise with minimal smoothing, and limiting the loss of data at the edges of the clouds (because the SG filtering requires a window with defined reflectivities or Doppler velocities around its center). All the gradients computed from the noisy reflectivities and Doppler velocities with the SG filter will be indicated with $\nabla_z \widetilde{Z}$ and $\nabla_z \widetilde{v}_{LoS}$. Correspondingly $\delta\widetilde{v}_{NUBF}$ and $\delta\widetilde{v}_{WS}$ will be the noisy estimates of the corrections proposed in Eqs. (10-11).

b. Case study with Medicane Apollo

The numerical weather prediction model adopted in this study is Weather and Research Forecasting (WRF) a next-generation mesoscale numerical weather prediction system designed to serve both operational forecasting and atmospheric research needs (Powers et al. 2017). The WRF model represents the atmosphere using multiple state variables that are discretized over consistent Cartesian grids. The model's solution is calculated through an explicit high-order Runge-Kutta time-split integration technique in the horizontal dimensions, with an implicit solver utilized for the vertical dimension. The case study under consideration is represented by Apollo, an intense Mediterranean tropical-like cyclone that affected many Mediterranean countries, especially Italy, in October 2021 (Borzì et al. 2022; Lagasio et al. 2022; Menna et al. 2023). In this study, WRF model version 3.9.1 has been adopted with 3 two-way nested domains at 3, 1 and 0.33 km grid spacing.WRF is configured with the following physical parameterizations: the RRTMG shortwave and longwave schemes (Mlawer et al. 1997; Iacono et al. 2008) are used for radiation; the Rapid Update Cycle (RUC) scheme is chosen as a multi-level soil model (6 levels) with higher resolution in the upper soil layer (0, 5, 20, 40, 160, 300 cm) (Smirnova et al. 1997, 2000); no cumulus scheme is activated in the three domains with grid spacings ranging from cloud-resolving to LES-like; finally, WRF Single–moment 6–class Scheme (WSM6, Hong et al. 2006) is adopted for microphysics. A TKE LES-like turbulence closure approach is adopted. The initial and boundary conditions are provided by Integrated Forecasting System (IFS) ECMWF at 9 km grid spacing and hourly temporal resolution for the 24 hours period from 29 to 30 October 2021, when the Apollo Medicane reached its high-intensity: a ship in the Mediterranean Sea passed through Apollo and measured a peak wind speed of 104 km/h (65 mph) and a pressure of 999.4 mb.

A scene simulated by the WRF model in correspondence to Medicane Apollo is here used to demonstrate the NUBF and wind shear effects. A 120° sector scan of WIVERN is shown in Fig. 5 with the red curved line representing the intersection of the antenna boresight with the ground. The satellite is in the ascending part of the orbit, with the radar scanning passing from the right side to the forward view. The corresponding vertical profiles of reflectivities and Doppler velocities are shown in the top panels of Fig. 6; both are averaged 1 km along track, thus they are very noisy (only 8 pulse pairs are averaged with an effective pulse repetition frequency of 4 kHz). Note that the reflectivities have been noise-subtracted; in addition ghosts have been identified and eliminated according to the methodology proposed by Rizik et al. (2023). The black line corresponds to the level where the signal to clutter ratio is equal to 10 dB; above that line the measurements can be confidently used to retrieve atmospheric properties. Note also the presence of a strongly attenuated region (azimuthal angle between 265° and 290°) with full extinction already at about 8 km. This is associated with a large amount of liquid content being lifted upwards by convective motions. The NUBF error (Δv_{NUBF}, left column) shows a characteristic variability between -2 and 2 m/s with larger errors at cloud egdes where the strongest reflectivity gradients are encountered. Note how the errors are more horizontally (vertically) stratified around $\phi = 360°$ ($\phi = 270°$) at forward view (side view) as expected from the discussion in Sect. 2. The NUBF errors are well predicted by Eq. (10). In presence of perfect estimates of reflectivity gradients results would have been excellent (third left panel). With real (noisy) measurements the NUBF error estimate are not as successful (bottom left panel); in addition the SG window implies that at the edges no estimate is possible because the gradients cannot be estimated (compare the narrower field where a correction can be estimated in the bottom with the upper panels).

The wind shear errors (second row, right panel) are generally smaller than the NUBF errors. In addition, since both strong reflectivity gradients and strong wind shears must be simultaneously present to create significant errors, the wind shear errors are generally present only at cloud edges. For instance, although there is a strong wind shear at about 5 km between azimuthal angles between 290° and 310° (top right panel) the wind shear error is lower than 0.5 m/s in that region because correspondingly there is not a large reflectivity vertical gradient. Overall, Eq. (11) properly capture the behaviour of the wind shear error.

c. Statistical results

In order to draw statistically robust conclusions about the NUBF and the wind shear errors and their corrections, the end to end simulator has been applied to a variety of meteorological scenes (in addition to Medicane Apollo, simulations of hurricane Milton and Elsa are included as well) for a total of more than 120,000 profiles in cloudy conditions (defined by integrated hydrometeor contents exceeding 100 g/m^2), which correspond to a total of more than 5,7 million sampled points (back-scattering volumes) with a signal-to-noise ratio (SNR) larger than 0 dB (i.e. for WIVERN reflectivities exceeding -18 dBZ) and with a signal to clutter ratio (SCR) larger than 10 dB. A

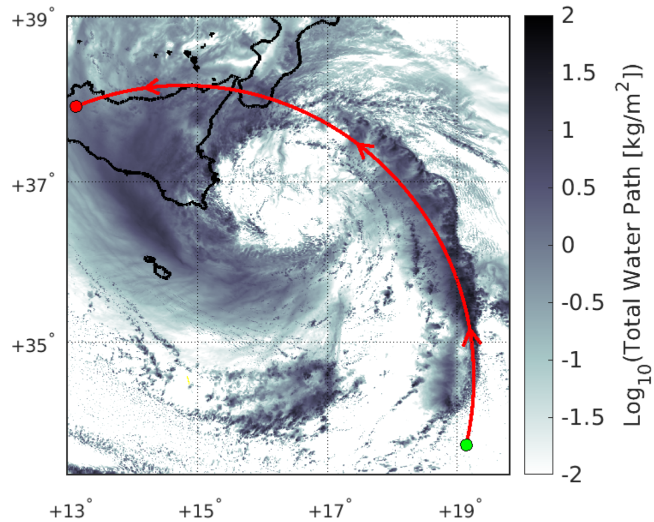

Fig. 5. A 120° sector WIVERN scan over Medicane Apollo for an ascending orbit with the green (red) circle corresponding to the side (forward) view. The grey color scale is modulated by the total hydrometeor water path in logarithmic scale.

density plot showing the distribution of Δv_{NUBF} as a function of the scanning angle ϕ from 0° to 360° for all the points of the simulated database characterized by SNR larger than 0 dB and by SCR larger than 10 dB is shown in Fig. 7. In addition, only the points in the $(n_H, n_V) = (3, 3)$ SG window have been included, in order to be more consistent with the statistical results shown later. The black lines correspond to different percentiles of the distribution, whose median value (red line) is, as expected, very close to 0 m/s. The most important feature is the broader (narrower) distribution of the errors close to forward- and backward-view (side-view) directions, which is expected because horizontal reflectivity gradients are typically smaller than vertical reflectivity gradients. This overcompensates for the greater Doppler fading that occurs at side views. Overall the 25^{th} and 75^{th} percentiles are of the order of ±0.4 m/s and ±0.1 m/s at forward/backward and side views whereas the 10^{th} and 90^{th} percentiles are of the order of ±0.9 m/s and ±0.3 m/s.

The median and the standard deviation for Δv_{NUBF} (indicated with σ_Δ) have been reported in Fig. 8 as a function of the azimuth angle (black continuous line in the left and right panel, respectively). Here the angles have been folded to the 0° - 90° interval because the errors are expected, when computed over a large number of profiles, to have forward/backward and left/right symmetries. As noted before the bias is essentially 0 for all angles (left panel) whereas σ_Δ ranges from 0.7 m/s to 0.4 m/s for forward/backward and side-view, respectively (right panel).

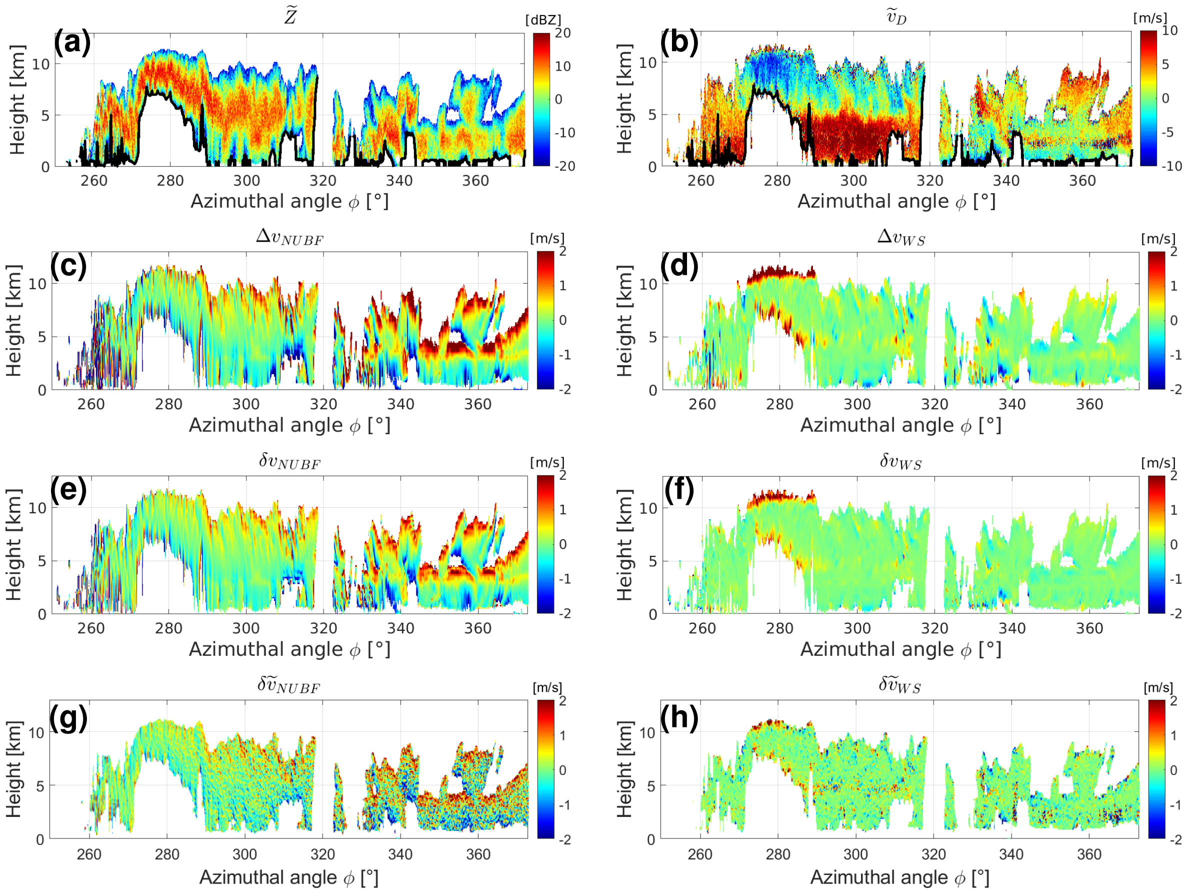

FIG. 6. Sector scan of Medicane Apollo with azimuthal angles ranging from 260° to 370° with the noise and ghost subtracted reflectivity (**a**) and the noisy LoS Doppler velocity (**b**). The black contour corresponds to a signal-to-clutter ratio of 10 dB. Regions with signal-to-noise ratio lower than 0 dB and with signal-to-clutter ratio under 10 dB have been removed in all the other panels. The Doppler velocity biases introduced by NUBF and wind shear are shown in the second row (**c** and **d**, respectively). The third and fourth rows depict the corrections for NUBF (**e**) and wind shear (**f**) computed by using ideal (i.e. without any noise) and noisy measurements (**g** and **h**, respectively).

The effectiveness of the NUBF correction has been tested by assuming a perfect knowledge of the gradients. After the NUBF correction, the reduction of the standard deviation of the histogram of $\Delta v_{NUBF} - \delta v_{NUBF}$ (indicated with $\sigma_{\Delta-\delta}$, blue line) with respect to σ_{Δ} (black line) is a measure of the effectiveness of the NUBF correction. There is a substantial improvement with a reduction

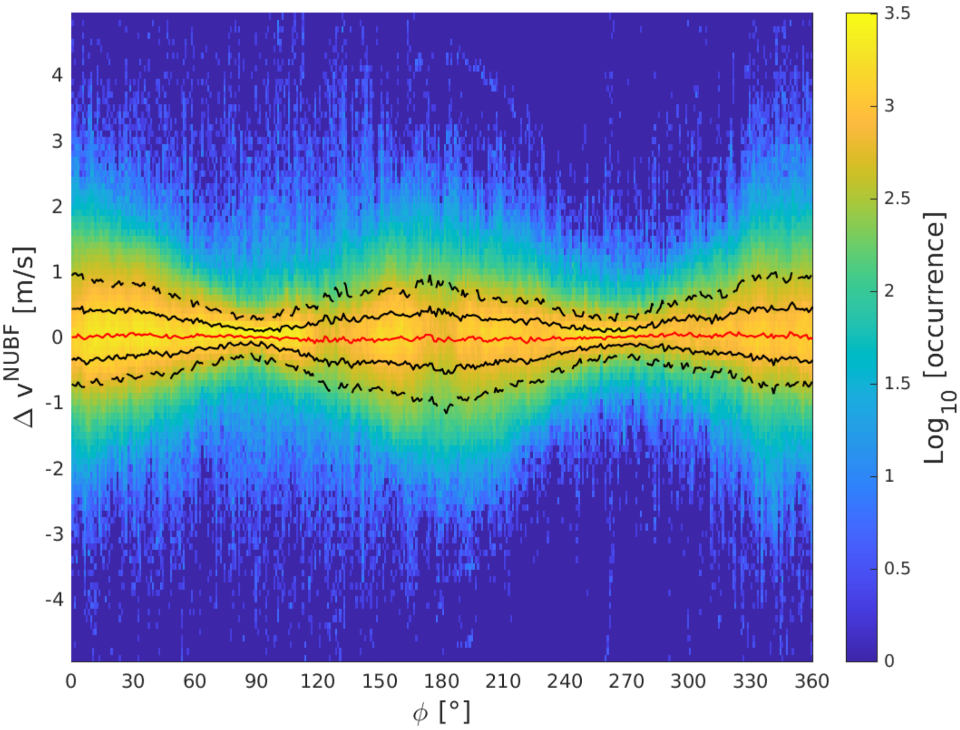

FIG. 7. Density plot for the NUBF error as a function of the azimuthal angle with the median (red line), the 10^{th} and 90^{th} percentile (dashed black lines) and the first and third quartile (black lines). Only points with $SNR > 0$ dB, $SCR > 10$ dB and from the domain of the $(n_H, n_V) = (3, 3)$ SG window have been considered.

of the error to 0.25 and 0.4 m/s at side-view and at forward/backward-views. This provides a limit for the best possible reduction of NUBF.

The correction will be less effective when using real measurements. In fact, the estimate of the gradients via SG smoothing will have two major drawbacks:

1. It will limit the region in which gradients are estimated to a sub-domain compared to the initial domain; this effect will be greater for larger SG windows, particularly when broadening the vertical window;

2. the use of noisy measurements will introduce additional uncertainties in estimating the gradients.

Different SG windows have been used: $(n_H, n_V) = (3, 3)$, $(3, 5)$, $(3, 7)$, $(3, 9)$, $(5, 3)$, $(5, 5)$, $(5, 7)$, $(5, 9)$, where the first (second) is the number of pixels in the horizontal (vertical) dimension,

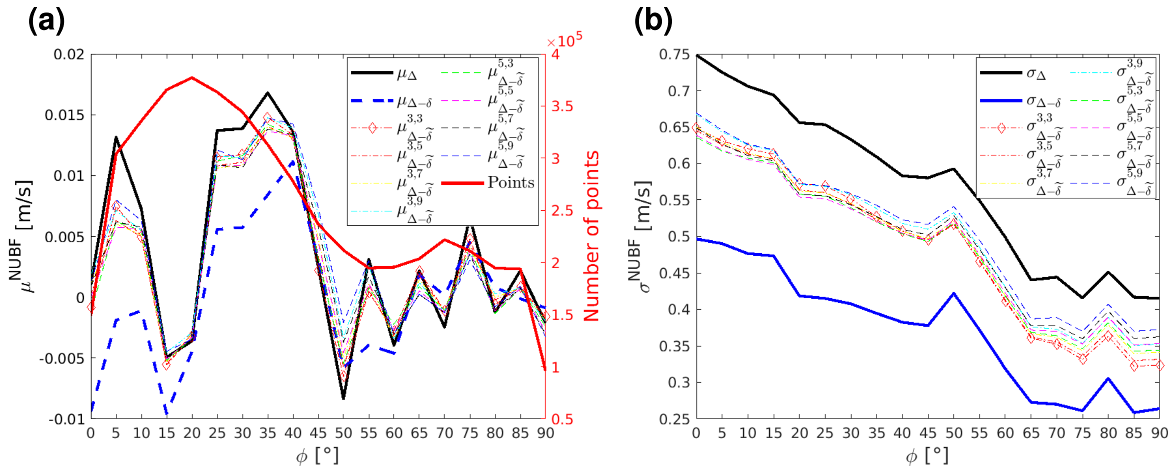

FIG. 8. Bias (**a**) and standard deviation (**b**) as a function of the azimuthal angle for the NUBF error (black line), and for the residual after the NUBF correction computed without noise (blue line) and with noise by using different SG windows (see legend). One pixel in the horizontal (vertical) corresponds to 1 km (167 m). All results are computed with the domain defined by the $(n_H, n_V) = (3, 3)$ SG window. The number of points for conducting the statistical analysis is plotted on the left panel (red curve, right y-axis).

each with a resolution of 1 km (0.125 km). For each SG window, the residual bias and standard deviations are computed as the bias and standard deviation of the histogram defined by: $\Delta v_{NUBF} - \delta\widetilde{v}_{NUBF}$ in the SG domain and by Δv_{NUBF} in the remaining domain (if any). These quantities will be indicated as $\sigma^{n_H, n_V}_{\Delta-\widetilde{\delta}}$ and are plotted as dashed and dash-dotted colored lines in Fig. 8. For the biases (left panel) there is no significative variation (all biases remain smaller than 3 cm/s). For the standard deviations (right panel), all SG curves are elevated with respect to the continuous blue line, as expected; none produces larger errors than the original error (black line), a sign that the correction is always worth doing. Overall, $\sigma^{3,3}_{\Delta-\widetilde{\delta}}$ produces the best results by reducing the NUBF error from 0.75 to 0.65 m/s at forward/backward view and from 0.43 to 0.32 m/s at side view. The improvement is robust for the selection of the SG window, with minimal variations when adopting different SG windows.

For the wind shear correction, the histograms in Fig. 9 illustrate the true WS error Δv_{WS} (red curve), the residual error after the correction when using the true vertical gradients of the reflectivity and the Doppler velocity, $\Delta v_{WS} - \delta v_{WS}$ (blue line), and the difference with the approximation computed with the vertical gradients after SG filtering with the same window used for NUBF, $(n_H, n_V) = (3, 3)$, $\Delta v_{WS} - \delta\widetilde{v}_{WS}$. It can be noted that there is an improvement with the correction

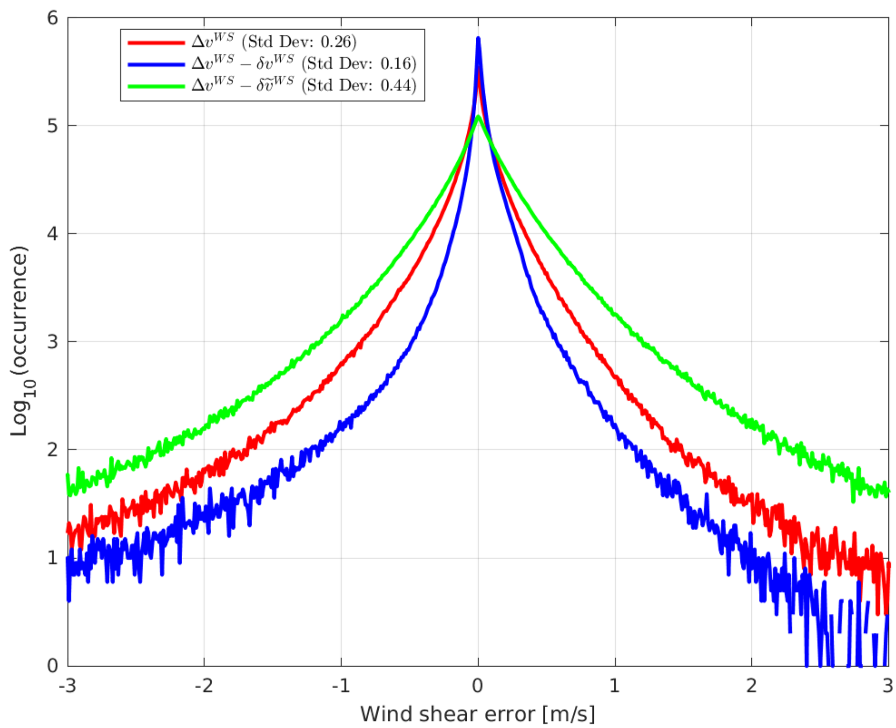

FIG. 9. Histogram for the distribution of the WS error (red curve) and for the residuals after the correction with the true gradients (blue curve) and after the correction with the gradients computed with the SG estimated gradients (green curve). Only points with $SNR > 0$ dB, $SCR > 10$ dB and corresponding to the domain of the $(n_H, n_V) = (3, 3)$ SG window have been considered.

performed when adopting in Eq. (11) the true gradients, with the standard deviation passing from 0.26 m/s for σ_{Δ}^{WS} to 0.16 m/s for $\sigma_{\Delta-\delta}^{WS}$. On the other hand the correction after SG filtering, $\sigma_{\Delta-\tilde{\delta}}^{WS^{3,3}}$, worsen the result by broadening the standard deviation to 0.44 m/s. This lack of improvement is due to the fact that in Eq. (11) there is a multiplication of two gradients, that tends to amplify the noise in the estimate of such quantities. This differs from the correction proposed for NUBF error in Eq. (9), which is linearly proportional to the reflectivity gradients.

5. Conclusions

Thanks to the recently launched EarthCARE mission, spaceborne Doppler atmospheric radars on board low-Earth orbiting satellites are now a reality, with several missions, either selected or under selection, now proposing Doppler capabilities (Battaglia et al. 2020). Measuring the speed of atmospheric targets from a fast moving platform presents several challenges. One potentially detrimental contribution relates to errors associated with the fact that the radar backscatter volumes may not be uniformly filled by atmospheric targets. Mitigation strategies have been developed in the past for nadir-looking radars and are currently being tested by the EarthCARE CPR.

This paper discusses the extension of NUBF correction techniques based on the reflectivity gradient method from nadir-looking to slant-looking Doppler radars, as recently proposed by the WIVERN ESA Earth Explorer 11 mission. Results based on a considerable number of simulations suggest that for the planned WIVERN mission, the NUBF errors will generally be well below 1 m/s for all viewing angles, but with larger errors expected when looking in the same direction as the satellite's motion. The correction developed in this study could potentially reduce the NUBF error by 40% with respect to the initial error. However, due to the noisiness of the estimates of the reflectivity gradients, the errors will only be reduced to values between 0.65 and 0.35 m/s in forward/backward and side view, respectively.

Wind shear across the backscattering volume also introduces errors, which have distributions with zero mean and standard deviation smaller than 0.3 m/s. While a theoretical framework for a correction based on the product of reflectivity and Doppler velocity vertical gradients has been developed, this correction, when applied to data with the noisiness expected for the WIVERN data, is actually worsening results and therefore it is not expected to be implemented in the mission Level-2 processing. Overall, the combination of wind shear and NUBF errors have distributions with no bias and standard deviations below 1 m/s (which was the requirement specified by WIVERN (2023)), i.e. considerably less than the noise error associated with the pulse pair estimator. The mission requirements can be satisfactorily met.

Although the methodology presented in this paper has been applied to the specific WIVERN mission, the framework for the NUBF and wind shear corrections is general and can be applied to any future mission deploying a slant-looking Doppler atmospheric radar.

Acknowledgments. The work by R. Rabino and A. Battaglia has been funded by the Italian Space Agency (ASI) project "Scientific studies for the Wind Velociy Radar Nephoscope (WIVERN) mission" (Project number: 2023-44-HH.0). The work by F. Tridon has been supported by the European Space Agency under the "End-to-End Performance Simulator Activity of the WIVERN Mission" (ESA Contract Number 4000139446/22/NL/SD). This research used the Mafalda cluster at Politecnico di Torino.

Data availability statement. All simulations can be make freely available upon request to the corresponding author.

References

Battaglia, A., 2021: Impact of second-trip echoes for space-borne high-pulse-repetition-frequency nadir-looking w-band cloud radars. *Atm. Meas. Tech.*, **14 (12)**, 7809–7820, https://doi.org/10.5194/amt-14-7809-2021, URL https://amt.copernicus.org/articles/14/7809/2021/.

Battaglia, A., R. Dhillon, and A. Illingworth, 2018: Doppler W-band polarization diversity space-borne radar simulator for wind studies. *Atm. Meas. Tech.*, **11 (11)**, 5965–5979, https://doi.org/10.5194/amt-11-5965-2018, URL https://www.atmos-meas-tech.net/11/5965/2018/.

Battaglia, A., and P. Kollias, 2014: Using ice clouds for mitigating the EarthCARE Doppler radar mispointing. *IEEE Trans. Geosci. Remote Sens.*, **53 (4)**, 2079–2085, doi: 10.1109/TGRS.2014.2353219.

Battaglia, A., and P. Kollias, 2015: Error Analysis of a Conceptual Cloud Doppler Stereoradar with Polarization Diversity for Better Understanding Space Applications. *J. Atmos. Ocean Technol.*, **32 (7)**, 1298–1319, https://doi.org/10.1175/JTECH-D-14-00015.1, URL https://doi.org/10.1175/JTECH-D-14-00015.1, https://doi.org/10.1175/JTECH-D-14-00015.1.

Battaglia, A., P. Martire, E. Caubet, L. Phalippou, F. Stesina, P. Kollias, and A. Illingworth, 2022: End to end simulator for the wivern w-band doppler conically scanning spaceborne radar. *Atm. Meas. Tech.*, **2021**, 1–31, https://doi.org/10.5194/amt-2021-342, URL https://amt.copernicus.org/preprints/amt-2021-342/.

Battaglia, A., A. Rizik, F. Tridon, and I. Isakeneta, 2025: I and Qs simulation and processing envisaged for space-borne polarisation Diversity Doppler Radars. *IEEE Trans. Geosci. Remote Sens.*, 1–1, https://doi.org/10.1109/TGRS.2025.3529672.

Battaglia, A., S. Tanelli, and P. Kollias, 2013: Polarization Diversity for Millimeter Spaceborne Doppler Radars: An Answer for Observing Deep Convection? *J. Atmos. Ocean Technol.*, **30 (12)**, 2768–2787, https://doi.org/10.1175/JTECH-D-13-00085.1, URL https://doi.org/10.1175/JTECH-D-13-00085.1, https://doi.org/10.1175/JTECH-D-13-00085.1.

Battaglia, A., and Coauthors, 2020: Spaceborne cloud and precipitation radars: Status, challenges, and ways forward. *Reviews of Geophysics*, **58 (3)**, e2019RG000 686, https://doi.org/10.1029/2019RG000686, URL https://agupubs.onlinelibrary.wiley.com/doi/abs/10.1029/2019RG000686, e2019RG000686 10.1029/2019RG000686, https://agupubs.onlinelibrary.wiley.com/doi/pdf/10.1029/2019RG000686.

Borzì, A. M., and Coauthors, 2022: Monitoring extreme meteo-marine events in the mediterranean area using the microseism (medicane apollo case study). *Scientific Reports*, **12 (1)**, 21 363.

Durden, S. L., S. Tanelli, L. W. Epp, V. Jamnejad, E. M. Long, R. M. Perez, and A. Prata, 2016: System Design and Subsystem Technology for a Future Spaceborne Cloud Radar. *IEEE Geosci. Remote Sens. Lett.*, **13 (4)**, 560–564, https://doi.org/10.1109/LGRS.2016.2525718.

Galfione, A., A. Battaglia, and P. Kollias, 2025: First insight into deep convective cloud observations by the earthcare doppler radar. *Atm. Meas. Tech. Disc.*, submitted.

Horanyi, A., C. Cardinali, M. Rennie, and L. Isaksen, 2014: The assimilation of horizontal line-of-sight wind information into the ECMWF data assimilation and forecasting system. Part I: The assessment of wind impact. *Quart. J. Roy. Meteor. Soc.*, **141**, 1223–1232, http://dx.doi.org/10.1002/qj.2430.

Iacono, M. J., J. S. Delamere, E. J. Mlawer, M. W. Shephard, S. A. Clough, and W. D. Collins, 2008: Radiative forcing by long-lived greenhouse gases: Calculations with the aer radiative transfer models. *Journal of Geophysical Research: Atmospheres*, **113 (D13)**.

Illingworth, A. J., and Coauthors, 2015: The EarthCARE Satellite: The Next Step Forward in Global Measurements of Clouds, Aerosols, Precipitation, and Radiation. *Bull. Amer. Met.*

Soc., **96 (8)**, 1311–1332, https://doi.org/10.1175/BAMS-D-12-00227.1, URL https://doi.org/10.1175/BAMS-D-12-00227.1, https://doi.org/10.1175/BAMS-D-12-00227.1.

Illingworth, A. J., and Coauthors, 2018: WIVERN: A New Satellite Concept to Provide Global In-Cloud Winds, Precipitation, and Cloud Properties. *Bull. Amer. Met. Soc.*, **99 (8)**, 1669–1687, https://doi.org/10.1175/BAMS-D-16-0047.1, URL https://doi.org/10.1175/BAMS-D-16-0047.1, https://doi.org/10.1175/BAMS-D-16-0047.1.

Kobayashi, S., H. Kumagai, and H. Kuroiwa, 2002: A Proposal of Pulse-Pair Doppler Operation on a Spaceborne Cloud-Profiling Radar in the W Band. *J. Atmos. Ocean Technol.*, **19**, 1294–1306, doi: http://dx.doi.org/10.1175/1520-0426(2002)019<1294:APOPPD>2.0.CO;2.

Kollias, P., A. Battaglia, K. Lamer, B. P. Treserras, and S. A. Braun, 2022a: Mind the gap - part 3: Doppler velocity measurements from space. *Frontiers in Remote Sensing*, **3**, https://doi.org/10.3389/frsen.2022.860284, URL https://www.frontiersin.org/article/10.3389/frsen.2022.860284.

Kollias, P., B. Puidgomènech Treserras, A. Battaglia, P. Borque, and A. Tatarevic, 2022b: Processing reflectivity and doppler velocity from earthcare's cloud profiling radar: the c-fmr, c-cd and c-apc products. *EGUsphere*, **2022**, 1–25, https://doi.org/10.5194/egusphere-2022-1284, URL https://egusphere.copernicus.org/preprints/2022/egusphere-2022-1284/.

Kollias, P., S. Tanelli, A. Battaglia, and A. Tatarevic, 2014: Evaluation of EarthCARE Cloud Profiling Radar Doppler Velocity Measurements in Particle Sedimentation Regimes. *J. Atmos. Ocean Technol.*, **31 (2)**, 366–386, https://doi.org/10.1175/JTECH-D-11-00202.1, URL https://doi.org/10.1175/JTECH-D-11-00202.1, https://doi.org/10.1175/JTECH-D-11-00202.1.

Lagasio, M., and Coauthors, 2022: A complete meteo/hydro/hydraulic chain application to support early warning and monitoring systems: the apollo medicane use case. *Remote Sensing*, **14 (24)**, 6348.

Manconi, F., A. Battaglia, and P. Kollias, 2024: Characterization of surface clutter signal in presence of orography for a spaceborne conically scanning w-band doppler radar. *EGUsphere*, **2024**, 1–22, https://doi.org/10.5194/egusphere-2024-2779, URL https://egusphere.copernicus.org/preprints/2024/egusphere-2024-2779/.

Manconi, F., P. Martire, F. Stesina, and A. Battaglia, 2025: High accuracy attitude determination of a spacecraft with a fast-rotating doppler radar reflector. *Acta Astronautica*, accepted for publication.

Menna, M., and Coauthors, 2023: A case study of impacts of an extreme weather system on the mediterranean sea circulation features: Medicane apollo (2021). *Scientific Reports*, **13 (1)**, 3870.

Mlawer, E. J., S. J. Taubman, P. D. Brown, M. J. Iacono, and S. A. Clough, 1997: Radiative transfer for inhomogeneous atmospheres: Rrtm, a validated correlated-k model for the longwave. *Journal of Geophysical Research: Atmospheres*, **102 (D14)**, 16 663–16 682.

Pazmany, A. L., J. C. Galloway, J. B. Mead, I. Popstefanija, R. E. McIntosh, and H. W. Bluestein, 1999: Polarization Diversity Pulse-Pair Technique for Millimeter-WaveDoppler Radar Measurements of Severe Storm Features. *J. Atmos. Ocean Technol.*, **16 (12)**, 1900–1911, https://doi.org/10.1175/1520-0426(1999)016⟨1900:PDPPTF⟩2.0.CO;2, URL https://doi.org/10.1175/1520-0426(1999)016⟨1900:PDPPTF⟩2.0.CO;2, https://doi.org/10.1175/1520-0426(1999)016⟨1900:PDPPTF⟩2.0.CO;2.

Powers, J. G., and Coauthors, 2017: The weather research and forecasting model: Overview, system efforts, and future directions. *Bulletin of the American Meteorological Society*, **98 (8)**, 1717–1737.

Rizik, A., A. Battaglia, F. Tridon, F. E. Scarsi, A. Kötsche, H. Kalesse-Los, M. Maahn, and A. Illingworth, 2023: Impact of crosstalk on reflectivity and doppler measurements for the wivern polarization diversity doppler radar. *IEEE Transactions on Geoscience and Remote Sensing*, **61**, 1–14, https://doi.org/10.1109/TGRS.2023.3320287.

Savitzky, A., and M. J. Golay, 1964: Smoothing and differentiation of data by simplified least squares procedures. *Analytical chemistry*, **36 (8)**, 1627–1639.

Schutgens, N. A. J., 2008: Simulated Doppler Radar Observations of Inhomogeneous Clouds: Application to the EarthCARE Space Mission. *J. Atmos. Ocean Technol.*, **25 (9)**, 1514–1528, doi: 10.1175/2007JTECHA1026.1.

Smirnova, T. G., J. M. Brown, and S. G. Benjamin, 1997: Performance of different soil model configurations in simulating ground surface temperature and surface fluxes. *Monthly Weather Review*, **125 (8)**, 1870–1884.

Smirnova, T. G., J. M. Brown, S. G. Benjamin, and D. Kim, 2000: Parameterization of cold-season processes in the maps land-surface scheme. *Journal of Geophysical Research: Atmospheres*, **105 (D3)**, 4077–4086.

Sy, O. O., S. Tanelli, N. Takahashi, Y. Ohno, H. Horie, and P. Kollias, 2014: Simulation of EarthCARE Spaceborne Doppler Radar Products Using Ground-Based and Airborne Data: Effects of Aliasing and Nonuniform Beam-Filling. *IEEE Trans. Geosci. Remote Sens.*, **52 (2)**, 1463–1479, https://doi.org/10.1109/TGRS.2013.2251639.

Tanelli, S., Z. S. Haddad, E. Im, S. L. Durden, O. O. Sy, E. Peral, G. A. Sadowy, and M. Sanchez-Barbetty, 2018: Radar concepts for the next generation of spaceborne observations of cloud and precipitation processes. *IEEE Proceedings of Radar Conference, Oklahoma City, OK*.

Tanelli, S., E. Im, S. L. Durden, L. Facheris, and D. Giuli, 2002: The Effects of Nonuniform Beam Filling on Vertical Rainfall Velocity Measurements with a Spaceborne Doppler Radar. *J. Atmos. Ocean Technol.*, **19 (7)**, 1019–1034, https://doi.org/10.1175/1520-0426(2002)019⟨1019:TEONBF⟩2.0.CO;2, URL https://doi.org/10.1175/1520-0426(2002)019⟨1019:TEONBF⟩2.0.CO;2, https://doi.org/10.1175/1520-0426(2002)019⟨1019:TEONBF⟩2.0.CO;2.

Tanelli, S., and Coauthors, 2014: Retrievals of microphysical parameters from recent apr-2 field experiments. *Precipitation Measuring Mission Science Team Meeting*, PMM Science Team Meeting, 4-8 August, Annapolis, MA.

Treserras, B., P. Kollias, A. Battaglia, S. Tanelli, H. Nakatsuka, and Y. Ohno, 2025: EarthCARE's Cloud Profiling Radar Antenna Pointing Correction using Surface Doppler Measurements. *J. Atmos. Ocean Technol.*, submitted.

WIVERN, M., 2023: Wivern report for assessment. Tech. rep., ESA-EOPSM-WIVE-RP-4375. Available at https://eo4society.esa.int/event/earth-explorer-11-user-consultation-meeting/.